



Efficiency of Surface Monitoring Layouts for Retrieving Accurate Moment Tensors in Hydraulic Fracturing Experiments

YI REN,¹ VÁCLAV VAVRYČUK,^{2,3}  YONGTAO GAO,¹ SHUNCHUAN WU,¹ and YIXIONG GAN⁴

Abstract—We study the sensor layouts of surface monitoring systems for injection areas in hydraulic fracturing experiments, which maximize the accuracy of retrieved moment tensors. The moment tensors (MTs) are determined using noisy synthetic P-wave amplitudes of microearthquakes with varying mechanisms. An optimum sensor layout is searched by minimizing a difference between the true and inverted MTs. First, we tested the efficiency of the circular networks. We focused on one-circle and two-circle layouts of various sizes and numbers of sensors on each circle and with their centre in the epicentral region. The results show that the optimal layout for events distributed within a circular epicentral area is characterized by: (1) one sensor fixed in the centre of the area; (2) about 1/10 of the total number of sensors gathered near the centre; and (3) the rest of sensors evenly distributed on a circle surrounding the area with the take-off angle of 135°. In homogeneous media, this angle corresponds to the radius of the circle comparable with depth of microearthquakes. Second, we compared the efficiency of the circular layout with other layouts: regular-grid, star-shaped and uniform focal-sphere layouts. Taking 25 sensors and 81 sensors as examples, we show that the two-circle layout is always the best, which means that we can achieve more accurate MTs using the circular layout than with other layouts, if the number of sensors in the experiment is fixed. This contradicts a common opinion that networks, which cover the target area, work equally well irrespective of their layout.

Keywords: Surface monitoring, Moment tensor inversion, Circular arrays, Wave propagation, Microearthquakes.

1. Introduction

Microseismic monitoring using surface networks is popular because of its flexibility and low cost (Duncan, 2005). Their layouts can be designed for various purposes: to enhance the signal-to-noise ratio (SNR) of recorded waves, to detect low-magnitude seismic events or to provide their accurate locations, energy, focal mechanisms or seismic moment tensors (MTs). Each of these goals needs its own specific sensor layout in order to produce the most accurate results, and many authors have conducted research on the sensor arrangement designed for these individual purposes (Anikiev et al., 2014; Chambers et al., 2010; Chen et al., 2019; Eaton & Ferozideh, 2011; Eisner et al., 2009, 2010; Eyre & van der Baan, 2017; Mesimeri et al., 2021; Pesicek, 2016; Schweitzer et al., 2011; Staněk et al., 2017; Viegas et al., 2012; Wessels et al., 2011; Zhang et al., 2011).

With respect to determining accurate focal mechanisms and MTs, various surface monitoring systems were compared or evaluated (Duncan & Eisner, 2010; Ren et al., 2020; Šílený, 2009; Staněk et al., 2014). Šílený (2009) showed that determining accurate non-double-couple (non-DC) components of MTs in local studies is data demanding and needs a dense station configuration, if errors in the event location and velocity profile are realistic. Duncan and Eisner (2010) described history and practice of the regular-grid and star-pattern surface and near-surface networks for reservoir monitoring. Staněk et al. (2014) showed that a star-like surface network provides a very stable inversion up to a very high level of noise in data. Eyre and van der Baan (2017) compared the reliability of MT solutions from a star-like surface network and two- and three-borehole arrays.

Supplementary Information The online version contains supplementary material available at <https://doi.org/10.1007/s00024-022-03122-9>.

¹ Key Laboratory of Ministry for Efficient Mining and Safety of Metal Mines, University of Science and Technology, Beijing, Beijing 100083, China.

² Institute of Geology, The Czech Academy of Sciences, Rozvojová 269, 165 00 Prague 6, Czech Republic. E-mail: vv@ig.cas.cz

³ Institute of Geophysics, The Czech Academy of Sciences, Boční II/1401, 14131 Prague 4, Czech Republic.

⁴ Emergency Science Research Institute, Chinese Institute of Coal Science, Beijing 100013, China.

Ren et al. (2020) showed that the offset-to-depth ratio R is an important parameter in the regular-grid surface monitoring. Under the influence of noise and location errors, a sensor layout with an optimum ratio R can significantly improve the accuracy of the MT inversion.

In summary, the authors showed that the surface monitoring in field experiments and in situ studies could obtain accurate MTs of microseismic events, when a high number of sensors is used and the sensors densely cover the studied area. In some experiments, even thousands of sensors are used for data collection (Duncan & Eisner, 2010; Eisner et al., 2010; Staněk et al., 2014, 2017), when accurate MTs are to be determined. However, not all microseismic monitoring projects can use such a huge number of sensors. If the number of sensors is limited or the sensors are not arranged reasonably, the MT inversion results will not be satisfactory. Hence, an optimum sensor arrangement is crucial for achieving a high accuracy of MTs.

In addition to the most common regular-grid layout and star-shaped layout, the form of circular or ring layouts has also been applied or studied in projects of various scales, such as the NORSAR in southern Norway, ARCES in northern Norway, GERES in southeast Germany and the local FORGE seismic network in southcentral Utah, etc. (Bungum et al., 1971; Mesimeri et al., 2021; Pankow et al., 2020; Schweitzer et al., 2011). Even though these circular layouts differ in the number of circles, the number of sensors, the layout span and the main research purpose, it is clear that the circular layouts have a great potential.

Aiming at designing a cost-effective surface network for determining high-resolution MTs, we test the efficiency of various sensor layouts under the condition of a limited number of sensors. We continue in the work of Ren et al. (2020), in which the efficiency of the regular-grid networks is studied. Here, we extend this work and study the efficiency of other sensor layouts. We focus on a seismicity produced by injection of fluids in hydraulic fracturing experiments, where the position and depth of the focal area are known. In this case, it is not necessary

to deploy a high number of sensors covering uniformly a large area, but we can use a lower number of sensors and position them in a much more effective way. We start with a simple circular sensor network with one or two circles of sensors of a different radius and sensor density. After finding an optimum arrangement, we compare this layout with the regular-grid, star-shaped and uniform focal-sphere networks. Based on extensive testing, we show that a circular sensor layout is a good alternative for retrieving accurate MTs and we propose general rules for designing optimally arranged networks.

2. Methods

2.1. Calculation of Moment Tensors

Compared to the focal mechanism solutions from first-arrival polarities and the full-waveform inversion, the amplitude inversion is simple but still a very powerful method (Baig & Urbancic, 2010; Eyre & van der Baan, 2015; Vavryčuk et al., 2017). It is applicable even to complicated 3D structures, if the Green's functions are calculated by the ray theory (Červený, 2001). In addition, considering complexities and uncertainties in the propagation of S waves (Vavryčuk, 1997), only the P-wave amplitude inversion is often applied. In this way, we eliminate effects such as the shear-wave splitting, caustics and triplications frequently observed in the S waveforms in inhomogeneous, anisotropic media (Vavryčuk, 2003a, 2003b, 2007, 2008). These effects should be considered for the accurate MT inversion of the S waves but they are very difficult to model. By contrast, the P-wave inversion was proved to be robust and rather insensitive to an inaccurately known velocity model (Šílený & Vavryčuk, 2000, 2002; Stierle et al., 2014a, 2014b).

The moment tensor inversion is based on the following formula, which is valid for time-independent moment tensors of point sources:

$$\mathbf{u} = \mathbf{G}\mathbf{m}, \quad (1)$$

where \mathbf{m} is the moment vector composed of six components of moment tensor \mathbf{M} ,

$$\mathbf{m} = [M_{11}, M_{22}, M_{33}, M_{23}, M_{13}, M_{12}]^T, \quad (2)$$

\mathbf{u} is the $n \times 1$ vector, representing the vertical component of displacement amplitudes observed at sensors, and n is the number of observed amplitudes for a given event. \mathbf{G} is the $n \times 6$ Green's function space-derivative matrix, which represents the medium response between the sensor and the source:

$$\mathbf{G} = \begin{bmatrix} g^{(1)} \\ g^{(2)} \\ \dots \\ g^{(n)} \end{bmatrix} = \begin{bmatrix} G_1^{(1)} & G_2^{(1)} & G_3^{(1)} & G_4^{(1)} & G_5^{(1)} & G_6^{(1)} \\ G_1^{(2)} & G_2^{(2)} & G_3^{(2)} & G_4^{(2)} & G_5^{(2)} & G_6^{(2)} \\ \dots & \dots & \dots & \dots & \dots & \dots \\ G_1^{(n)} & G_2^{(n)} & G_3^{(n)} & G_4^{(n)} & G_5^{(n)} & G_6^{(n)} \end{bmatrix} \quad (3)$$

$G_k^{(i)}$ ($k = 1, 2, \dots, 6$) is the element of the Green's function matrix for the i -th vertical sensor:

$$\begin{cases} G_1^{(i)} = G_{13,1}^{(i)} \\ G_2^{(i)} = G_{23,2}^{(i)} \\ G_3^{(i)} = G_{33,3}^{(i)} \\ G_4^{(i)} = G_{23,3}^{(i)} + G_{33,2}^{(i)} \\ G_5^{(i)} = G_{13,3}^{(i)} + G_{33,1}^{(i)} \\ G_6^{(i)} = G_{23,1}^{(i)} + G_{13,2}^{(i)} \end{cases} \quad (4)$$

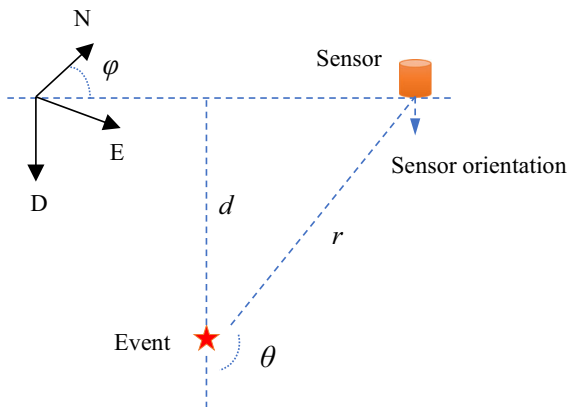


Figure 1

Sensor layout parameters of surface monitoring. Angle θ is the take-off angle (0° – 180°), angle φ is the azimuth (0° – 360°), d is depth of the event, r is the hypocentral distance between a sensor and the event

$G_{p3,m}$ is the spatial derivative $\partial G_{p3} / \partial x_m$ and G_{p3} is the vertical component of the amplitude at the receiver measured along the x_m -axis produced by the point force at the source directed along the x_p -axis. For surface monitoring (Fig. 1), we get the following form of components G_k (Pettitt, 1998; Pujol & Herrmann, 1990):

$$\begin{cases} G_1 = -\cos\theta \cdot S \cdot \sin^2\theta \cos^2\varphi / d \\ G_2 = -\cos\theta \cdot S \cdot \sin^2\theta \sin^2\varphi / d \\ G_3 = -\cos\theta \cdot S \cdot \cos^2\theta / d \\ G_4 = -\cos\theta \cdot S \cdot \sin 2\theta \sin\varphi / d \\ G_5 = -\cos\theta \cdot S \cdot \sin 2\theta \cos\varphi / d \\ G_6 = -\cos\theta \cdot S \cdot \sin^2\theta \sin 2\varphi / d \end{cases} \quad (5)$$

where $S = \frac{1}{4\pi\rho V_p}$, d is depth of the source and trigonometric functions of angles θ and φ reflect the radiation pattern of individual force couples of the source. It should be noted that the formula of $G_{k1,2}$ in Table 2.2 of Pettitt (1998) is wrong, and $G_{k1,2}$ should be equal to $\frac{1}{r_k} \cdot \sin^2 l_k \cdot \sin 2\phi_k$.

When inverting Eq. (1), we use the least-squares method to calculate the moment tensor:

$$\mathbf{M} = (\mathbf{G}^T \mathbf{G})^{-1} \mathbf{G}^T \mathbf{u}. \quad (6)$$

2.2. Definition of Moment Tensor Errors

In the synthetic tests, we assume a large number of random moment tensors. By setting the parameters of the medium, the theoretical first P-wave amplitudes at the sensors can be calculated. Then the amplitudes are disturbed by noise, and the moment tensor inversion is carried out again using the noisy amplitudes. The difference between the true MT and the MT retrieved using the noisy data is calculated as follows (Vavryčuk et al., 2017; Willemann, 1993):

$$E_{MT} = \frac{1}{N} \sum_{k=1}^N \arccos \left(\frac{1 M_{ij}^{(k,true)} M_{ij}^{(k,noisy)}}{2 M^{(k,true)} M^{(k,noisy)}} \right) \quad (7)$$

where E_{MT} is the average moment tensor error (also named MT error, in degrees) of N simulations for the same sensor layout, $i, j = 1, 2, 3$; $M_{ij}^{(k,true)}$ are the components of the k -th true moment tensor; $M_{ij}^{(k,noisy)}$ are the components of the k -th moment tensor inverted from noisy amplitudes, and quantities $M^{(k,true)}$ and $M^{(k,noisy)}$ are the scalar moments defined by their Euclidean norms:

$$\begin{aligned}
 M^{(k,true)} &= \sqrt{\frac{1}{2} M_{ij}^{(k,true)} M_{ij}^{(k,true)}}, \\
 M^{(k,noisy)} &= \sqrt{\frac{1}{2} M_{ij}^{(k,noisy)} M_{ij}^{(k,noisy)}}.
 \end{aligned}
 \tag{8}$$

The Einstein summation convention is applied to repeated indices i and j in Eqs. (7) and (8).

The main reason, why we choose to use E_{MT} calculated using Eqs. (7) and (8) is that this error metric can more comprehensively represent the change of MTs, because it reflects differences in the double-couple as well as in the non-double-couple parts of MTs. In addition, this metric is the most common metric applied to tensors. For double-couple focal mechanisms, the E_{MT} roughly corresponds to the angle of the source mechanism rotation. Besides, both the true MTs and noisy MTs are further decomposed according to Vavryčuk (2001, 2011) into the isotropic (ISO), double-couple (DC) and compensated linear vector dipole (CLVD) components. The DC percentage is often used as an indicator for a shear-tensile characteristic of seismic events. Therefore, we also evaluate the accuracy of the MT inversion by calculating uncertainties in the DC percentage (Ren et al., 2020; Šílený, 2009) as follows:

$$E_{DC} = \frac{1}{N} \sum_{k=1}^N \left| DC_{noisy}^k - DC_{true}^k \right|, \tag{9}$$

where E_{DC} is the average error of the DC component (also named DC error, in %) of N simulations for the same sensor layout; DC_{noisy}^k is the DC percentage of the k -th event calculated from noisy data, and DC_{true}^k is the true DC percentage of the k -th event.

2.3. Numerical Simulations

2.3.1 Source Simulations

In the optimization process, we use $N = 10,000$ random focal mechanisms for each type of the sensor layout and for each focal mechanism simulation. We add random noise with a uniform (flat) probability distribution between -10% and $+10\%$ of the maximum amplitude of all events recorded at the nearest sensor. In order to ensure the randomness of the

source mechanism selection, we use random MT components $M_{ij}^{(true)}$ ranging between -1 and 1 .

As the strike-slip events (with strike 45° , dip 90° and rake 0°) and the dip-slip events (with strike 45° , dip 90° and rake 90°) have been often studied by other authors (Eyre & van der Baan, 2017; Maxwell et al., 2010; Ren et al., 2020; Staněk et al., 2014; Wessels et al., 2011), we also simulate events with these two particular focal mechanisms. In this way, we check, whether the results deviate from those for the events with random focal mechanisms. Since focal mechanisms in active areas always display some variations, we do not fix the strike, dip, and rake angles, but we set a 10° fluctuation interval for all three angles. For strike-slip events, we use strikes between 40° – 50° , dips between 80° – 90° , and rakes between -5° and 5° . For dip-slip events, we use strikes between 40° – 50° , dips between 80° – 90° , and rakes between 85° – 95° . The slope angle α (the inclination of the slip vector from the fault) defines a tension/compression character of the shear-tensile event (Vavryčuk, 2001), and it is randomly selected between 0° – 90° both for strike-slip and dip-slip events. Event simulations are repeated in both two groups 10,000 times, respectively. The definition of moment tensor errors is the same as that of the random focal mechanisms.

2.3.2 Medium Simulations

In numerical simulations, we assume a homogeneous medium with density of 2700 kg/m^3 . The P-wave velocity is 5000 m/s , and the Poisson's ratio is 0.25 . The goal of this study is to perform synthetic tests, which compare the efficiency of different sensor layouts, hence using a more complicated model is not essential for this study. In addition, a homogeneous isotropic medium is often a good approximation in P-wave studies of the local microseismicity, where rays are close to straight lines and their take-off angles from the source do not significantly deviate from those in the homogeneous medium (Červený, 2001; Eide et al., 2018; Onnis & Carcione, 2017).

2.3.3 Sensor Layout Simulations

In the optimizing process of the circular layout, we assume all events fixed at depth of 1000 m directly below the central sensor in Sect. 3.1. In order to mimic a real situation, we further assume events randomly located in a cylinder (centroid: 0, 0, 1000 m; radius: 500 m; depth: from 900 to 1100 m) in Sect. 3.2 and Sect. 3.3. The size of this cylindrical area is similar to the range of 9 strongest microseismic events induced during hydraulic fracturing of the Montney Shale in Canada (Pesicek et al., 2016), where a rounded regular grid layout of sensor is deployed.

First, we consider a circular configuration of sensors, which is the simplest azimuthally symmetric sensor layout. The azimuthal symmetry is advantageous, because all azimuths are uniformly covered. The central sensor is prominent, because it constrains depth of foci and it is positioned in the centre of the focal sphere. Since this sensor is the nearest one, it is also the most sensitive sensor with a high SNR. This layout is, in particular, popular in monitoring seismicity in hydrofracturing, geothermal, and multi-azimuthal anisotropic experiments (Novitsky et al., 2018; Tsuji et al., 2011; Vavryčuk et al., 2004), and for detecting nanoseismicity (Wust-Bloch & Joswig, 2006). The design of the circular layout is divided into two steps: the optimization of one circle and the optimization of two circles. In order to ensure the stability of the inversion and the symmetry of the sensor layout, both circular layouts have one sensor fixed at the centre of the circle(s). For the tests, we take a total of 50 sensors of the network as an example (see Fig. 2); however, the results are basically the same also for other numbers of sensors larger than 6, which is the minimum number of sensors required for the P-wave amplitude inversion.

In both the one-circle and two-circle layouts, the sensors on each circle are evenly distributed according to the azimuth angle. For the two-circle layout, the number of sensors on Circle 1 and Circle 2 is changed during the optimization process. The number of sensors on the outer circle is not specified, but Circle 1 always has more sensors than Circle 2. We limit the take-off angle to sensors by varying the circles' radii to the interval of 120°-150° for Circle 1,

and to 120°-180° on Circle 2 in steps of 1°. Outside these intervals, the errors are quite high and not worth being analysed.

3. Results

3.1. Fixed Event Location

First, we assume random focal mechanisms of events with a fixed location at the centre of the sensor layouts at depth of 1000 m. Figure 3 shows the error E_{MT} corresponding to different take-off angles to the sensors for the one-circle layout shown in Fig. 2a. The total number of sensors is 50. When the take-off angle is around 131°, the E_{MT} is minimum being about 4.5°. The take-off angles ranging from 124° to 138° yield still a low error, which is smaller than 5°, but outside this angle interval, the MT error becomes significantly larger.

Since the one-circle layout only results in a single take-off angle, apart from the central sensor, we also consider a two-circle layout as shown in Fig. 2b. Since the total number of sensors is 50, we study various combinations of the number of sensors distributed on Circle 1 and Circle 2. We consider all possible combinations, but we show results only for some of them (Fig. 4).

Figure 4 shows the error E_{MT} of the two-circle layout within the specified range of take-off angles, when 2/6/10/14/18/22 sensors are set on Circle 2 (corresponding to 47/43/39/35/31/27 sensors on Circle 1). We conclude:

1. The take-off angles have a great influence on the E_{MT} in each combination. For the situations which are not included in Fig. 4, such as both the take-off angles to Circle 1 and Circle 2 are smaller than 110°, their E_{MT} are quite large and we do not show them in figures.
2. The minimum error E_{MT} corresponding to each combination varies. For example, the E_{MT} corresponding to 6 sensors on Circle 2 (Fig. 4b) is lower than 3.8°, but when 22 sensors are set on Circle 2 (Fig. 4f), the E_{MT} is higher than 4.5°.
3. The take-off angles of the two circles corresponding to the optimal layout vary for each combination. If the number of sensors is low on

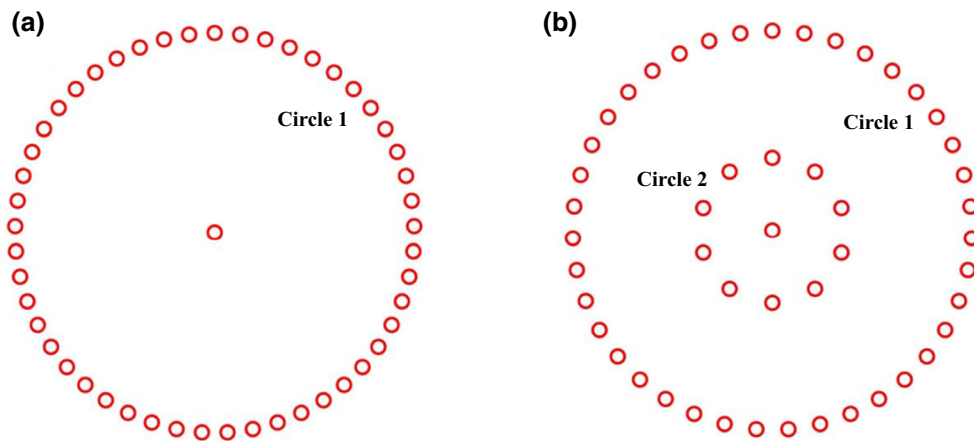


Figure 2
Scheme of the one-circle (a) and two-circle (b) layouts. The total number of sensors is 50

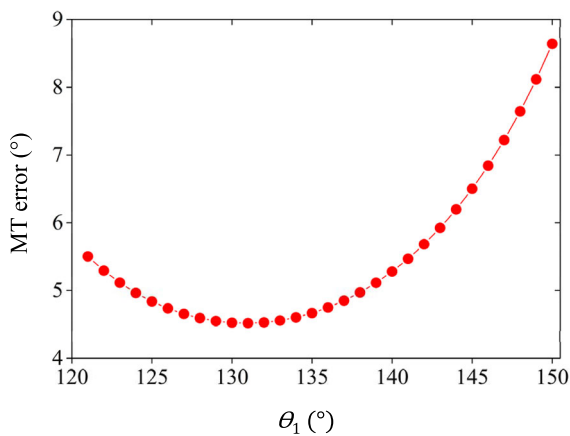


Figure 3

Error E_{MT} as a function of the take-off angle θ_1 for the one-circle layout

Circle 2 (Fig. 4a), the optimal layout is characterized by take-off angles of Circle 2 close to 180° . This means that the sensors are concentrated near the centre of the circle. The take-off angle corresponding to Circle 1 is about 135° . When the number of sensors is relatively high on Circle 2 (Fig. 4e), the optimal layout is characterized by take-off angles of 156° and 133° for Circle 2 and Circle 1, respectively.

Figure 5 summarizes the results for all sensor combinations. Figure 5a implies that setting too many or too few sensors on Circle 2 increases the error E_{MT} . The optimum number of sensors on Circle

2 is 5. Figure 5b shows the optimum take-off angles to the two circles corresponding to the optimum layout in each combination. The take-off angle corresponding to Circle 1 is always between 130° and 136° , but the take-off angle to Circle 2 varies. If the number of sensors on Circle 2 is less than 10, the take-off angles are close or equal to 180° . This means that the sensors on Circle 2 form a micro-array around the central sensor. If the number of sensors on Circle 2 is greater than 10, the radius of Circle 2 starts to increase.

A detailed behaviour of the E_{MT} for the optimum layout is shown in Fig. 6. The layout consists of 44 sensors on Circle 1, 5 sensors on Circle 2 and one central sensor. In our simulations, we assumed that noise is independent for each sensor. This limits the radius of Circle 2. The size of the micro-array of sensors around the central stations should be very small (with take-off angle close to 180°) but not smaller than a predominant wavelength of seismic noise. In this way, we ensure that observations on sensors of Circle 2 will not be influenced by noise in the same way.

3.2. Varying Event Location

Next, we simulate events randomly located in a cylindrical area (centroid: 0, 0, 1000 m; radius: 500 m; depth: from 900 to 1100 m). The other parameters remain unchanged. The minimum errors

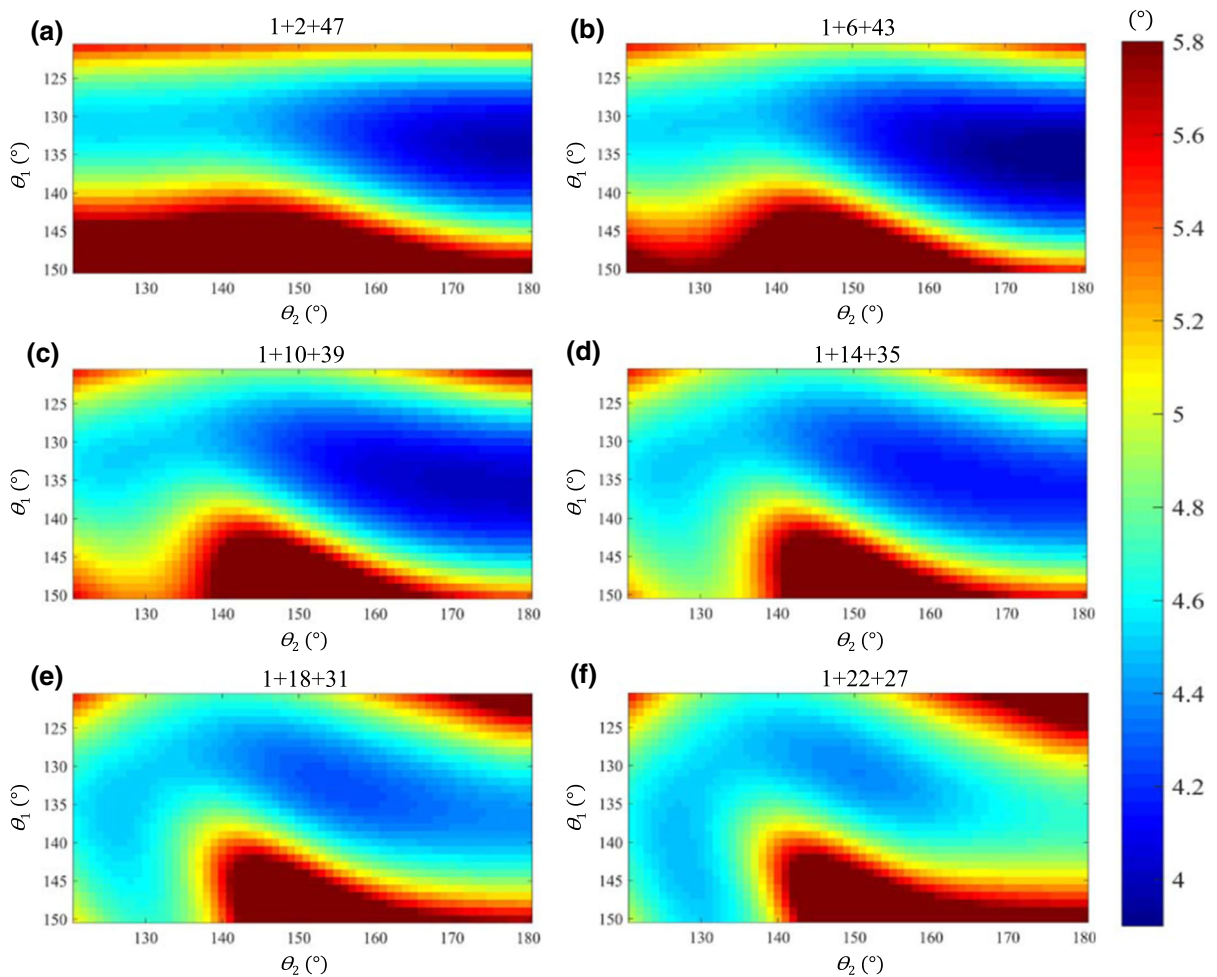


Figure 4

Error E_{MT} for the two-circle layout with various numbers of sensors on Circle 1 and Circle 2. (a) 1 + 2 + 47 means: one sensor fixed at the centre and 2 sensors on the inner circle (Circle 2) and 47 sensors on the outer circle (Circle 1). Quantities θ_1 and θ_2 are the take-off angles of Circle 1 and Circle 2, respectively. Figures representing other tested combinations are similar. The colour scale is in degrees

E_{MT} and E_{DC} are calculated for the two-circle layouts with 10–100 sensors and the corresponding optimal layout parameters are analysed.

Figure 7 shows minimum MT errors obtained with the optimal circular layout as a function of the number of sensors at Circle 2 and of the total number of sensors. The take-off angle to Circle 2 is 177° , which corresponds to a radius of 52 m. However, as seen in Fig. 6, other take-off angles in the range of 165° – 180° corresponding to the radius of Circle 2 between 0 and 260 m will work equally well. Figure 7 indicates that errors E_{MT} and E_{DC} gradually decrease as the number of sensors increases. The

decrease rate is fast for a low number of sensors and it becomes slower for a higher number of sensors. For example, increasing the number of sensors from 10 to 20, the E_{MT} error reduces considerably by nearly 3° . If we increase the number of sensors from 90 to 100, the E_{MT} error reduces by 0.2° only.

Compared with the minimum E_{MT} error of the optimal layout for events fixed at the centre in Fig. 5, the error of events with a varying location (within a cylinder with a diameter of 1000 m and a height of 200 m) has increased by about 0.5° when 50 sensors are used. Even if the foci range is further expanded,

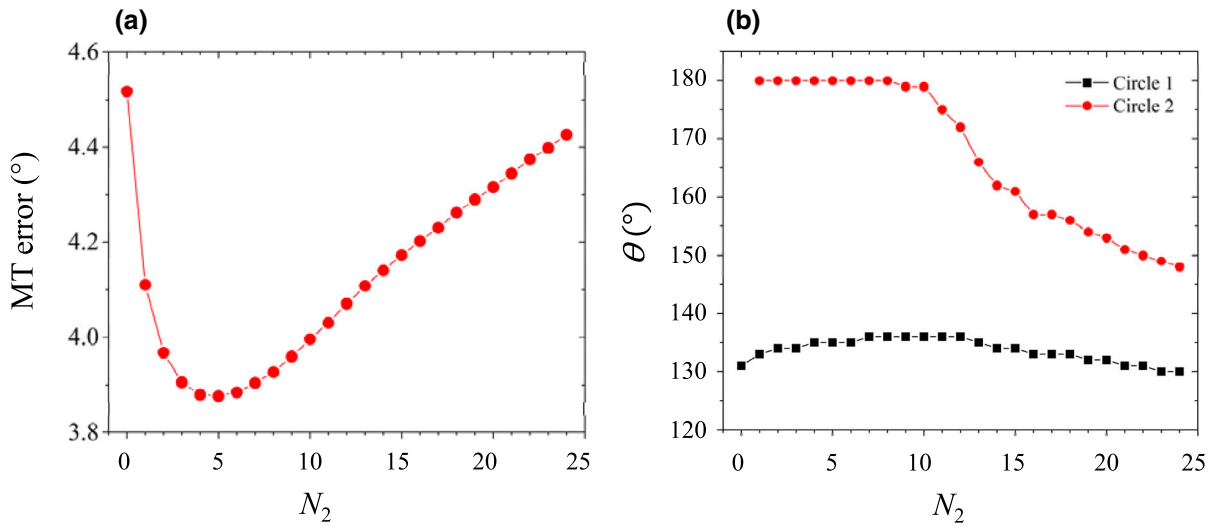


Figure 5

a The error E_{MT} as a function of the number of sensors on Circle 2 (N_2) for the two-circle layout. **b** The take-off angles of the two circles corresponding to the minimum E_{MT} in each combination. The event location is fixed

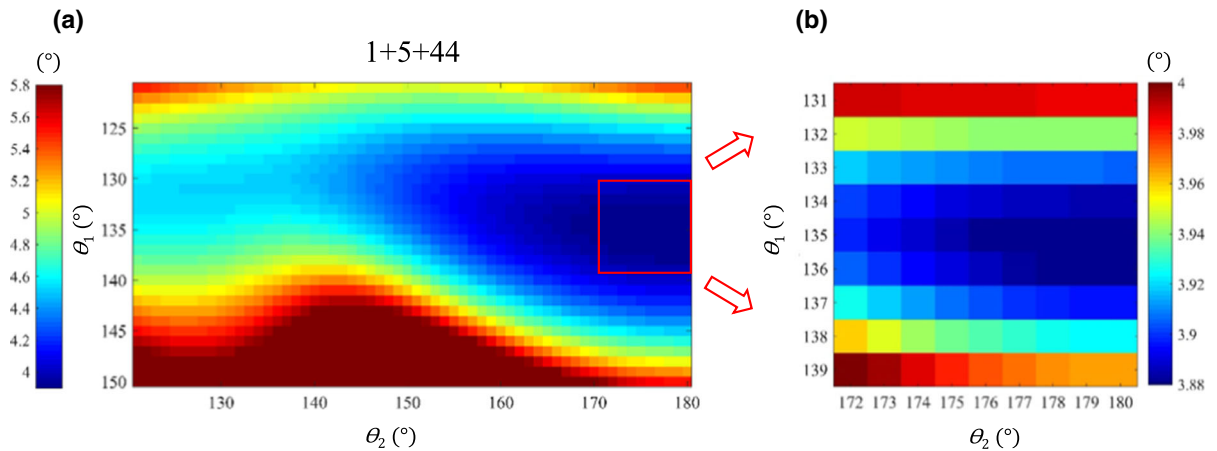


Figure 6

a The E_{MT} error as a function of take-off angles θ_1 and θ_2 , and **b** its detailed behavior for the two-circle layout 1 + 5 + 44

the efficiency of the MT inversion is not significantly changed.

Figure 7 also indicates the number of sensors on Circle 2 required for the optimal circular layout. This number is about 1/10 of the total number of sensors. However, because of noise in data and a rather shallow minimum of E_{MT} , the optimum sensor number may slightly vary. This is the reason why the red stars do not form exactly the straight line. These deviations can be considered as insignificant.

3.3. Comparison of the Circular Layout with Other Layouts

In surface monitoring, a regular-grid layout and a star-shaped layout of sensors have been studied and applied by many authors (Duncan & Eisner, 2010; Eyre & van der Baan, 2017; Ren et al., 2020; Staněk et al., 2014). Therefore, we compare the accuracy of the MT inversion between our proposed circular layout, a regular-grid layout and a star-shaped layout

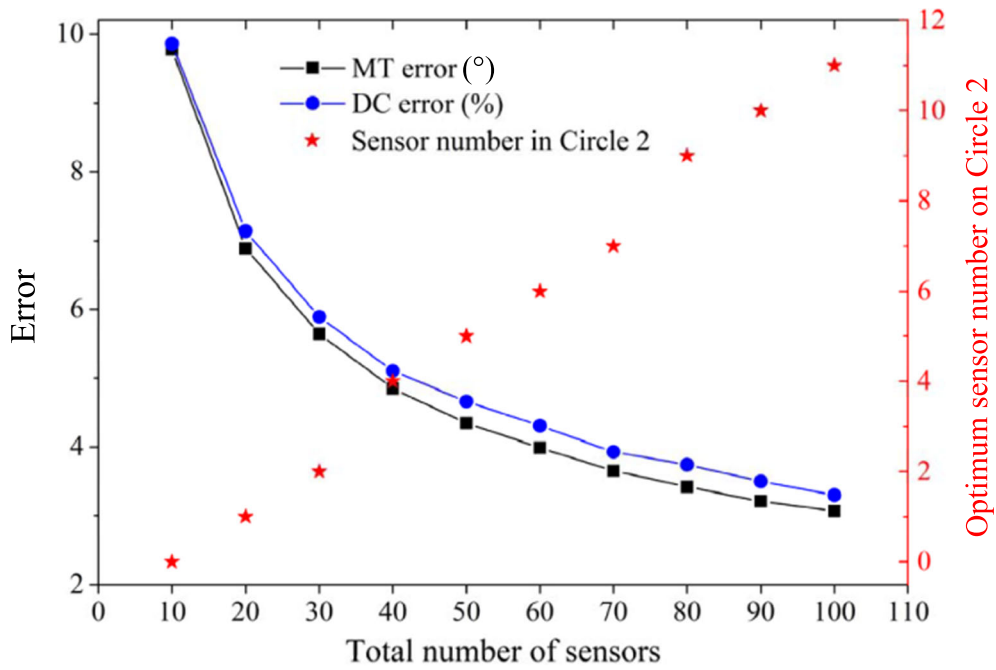


Figure 7

The minimum errors E_{MT} and E_{DC} as a function of the total number of sensors N . The optimum number of sensors on the inner circle (Circle 2) is indicated by red points for each sensor configuration

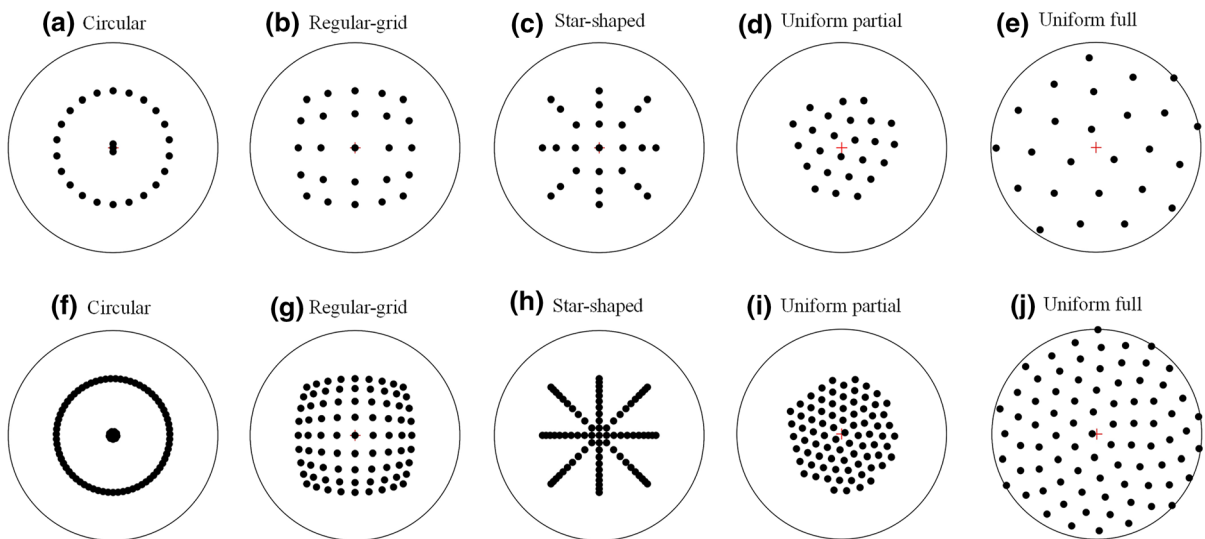


Figure 8

Focal sphere coverage of five different sensor layouts for the event located at the position (0, 0, 1000 m). Upper panels—layouts with 25 sensors, lower panels—layouts with 81 sensors. The red crosses mark the centres of the layouts. The outer circle in panels corresponds to the horizontal ray directions

Table 1
Errors and standard deviations of the MT inversion for different sensor layouts

Number of sensors	Error	Circular layout	Regular-grid layout	Star-shaped layout	Uniform partial focal-sphere layout	Uniform full focal-sphere layout
25 sensors	MT error (°)	6.46	6.59	7.03	8.01	8.80
	Std. dev. (°)	3.06	3.09	3.34	3.97	4.05
	DC error (%)	6.74	6.84	7.24	8.09	8.98
	Std. dev. (%)	5.73	5.78	6.16	6.93	7.46
81 sensors	MT error (°)	3.81	3.93	4.39	4.62	5.08
	Std. dev. (°)	1.84	1.89	2.17	2.33	2.38
	DC error (%)	4.09	4.19	4.67	4.89	5.45
	Std. dev. (%)	3.55	3.64	4.08	4.29	4.63

using 25 (Fig. 8a–e) and 81 sensors (Fig. 8f–j). The parameters of the medium and of events are the same as in the previous simulation with a varying event location.

The layouts are defined as follows (see Fig. 8): The circular layout is formed by 1 + 2 + 22 and 1 + 9 + 71 sensors, respectively. The regular-grid is formed by 5 × 5 and 9 × 9 sensors, and the star-shaped layout is formed by 3 × 8 + 1 and 10 × 8 + 1 sensors, respectively. For parameters of the regular-grid layout, we refer to Ren et al. (2020): the offset-to-depth ratio is set to 1, and all sensors are evenly arranged in a square with a side length twice the depth of the source. For parameters of the star-shaped layout, we refer to Eyre and van der Baan (2017). Each ‘arm’ of the network consists of 3 and 10 sensors spaced at 333 m and 100 m intervals, respectively.

In addition to the regular-grid on the surface, we also consider a uniform layout on the focal sphere, because studies mention that the uniform coverage of sensors on the focal sphere is important for determining accurate MTs (Eyre & van der Baan, 2015; Kwiatak et al., 2016; Pesicek et al., 2016; Šílený, 2009; Vavryčuk et al., 2017). The uniform focal-sphere layout is modelled using the publicly available Matlab code S2-Sampling-Toolbox (<https://github.com/AntonSemechko/S2-Sampling-Toolbox>). The code can generate an approximately uniform triangular tessellation of a unit sphere by minimizing generalized electrostatic potential energy of a system

of charged particles. Based on this code, we obtain the take-off angles and azimuth angles of the sensors that are almost evenly arranged either on the full focal sphere (Fig. 8e,j) or on a part of the focal sphere within the radius of Circle 1 (Fig. 8d,i). In addition, as it is unlikely that sensors collect all records in an engineering project, we assume that 2 and 15 amplitudes at randomly selected sensors are lost for the layouts of 25 and 81 sensors, respectively.

Table 1 shows layouts ordered according to both errors E_{MT} and E_{DC} as follows: circular layout < regular-grid layout < star-shaped layout < uniform partial focal-sphere layout < uniform full focal-sphere layout. The circular layout always behaves best, but the improvement is rather weak, the MT and DC errors of the circular layout being only about 0.1 (° or %) lower than those of the regular-grid layout. The advantage of the circular layout is more obvious with respect to the star-shaped layout and the uniform focal-sphere layouts. It seems surprising that the MT and DC errors and their standard deviations are always the largest for the uniform focal-sphere layouts. We will explain this phenomenon in the Discussion section. In addition, results for two other cases are provided in the Electronic Supplement; namely the case of using Gaussian noise (Table S1) and the case of using noise of uniform probability distribution without amplitude loss (Table S2). The results are basically consistent with Table 1.

The errors are calculated for a varying event location. In order to mimic real working conditions,

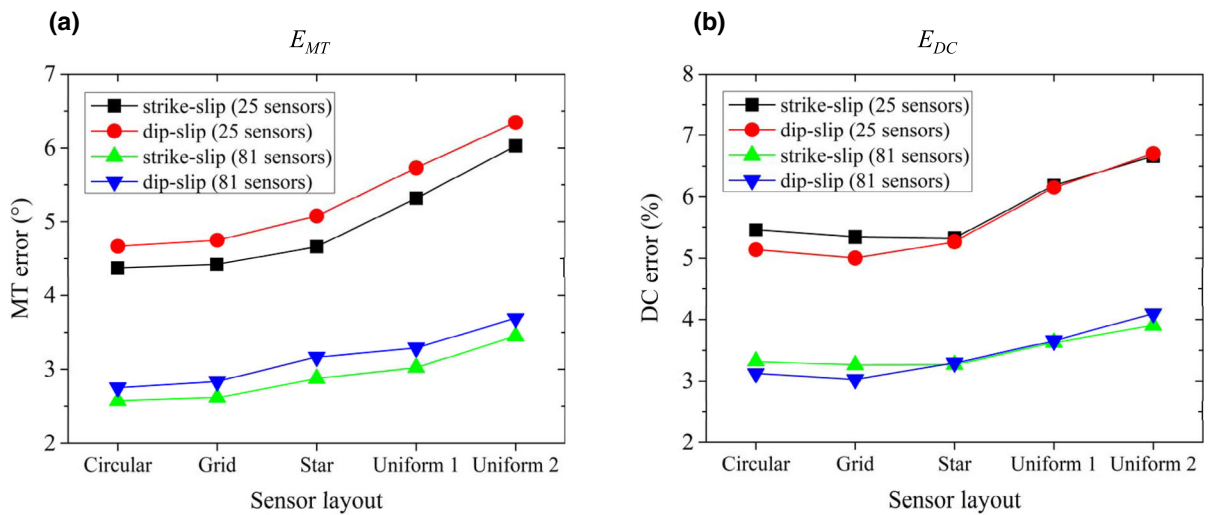


Figure 9

The errors corresponding to five different sensor layouts for two types of focal mechanisms (strike-slip and dip-slip) and for the varying event location when 25 sensors (2 randomly amplitudes are ignored) and 81 sensors (15 randomly selected amplitudes are ignored) are used, respectively. Uniform 1 and Uniform 2 mean the uniform partial and full focal-sphere layouts, respectively

the MT inversion is performed for incomplete data: amplitudes at 2 and 15 randomly selected sensors are ignored for the layout of 25 and 81 sensors, respectively.

In addition to the results of random focal mechanisms, Fig. 9 shows the errors of the MT inversion corresponding to five different sensor layouts for strike-slip and dip-slip events when using 25 or 81 sensors. Sensor layout parameters are the same as in Fig. 8, and events are randomly located in the cylindrical area. As far as the E_{MT} error is concerned, the circular layout always performs best irrespective of the type of the focal mechanism. The uniform partial as well as full focal-sphere layouts still perform the worst. The regular-grid layout is better than the star-shaped layout. The errors of dip-slip events are always higher than those of strike-slip

events irrespective of the layouts. The situation with E_{DC} error is more complicated. The circular layout no longer performs best. For strike-slip events, the star-shaped layout has the smallest error. But for dip-slip events, the smallest error belongs to the regular-grid layout. However, the differences are very tiny. There are three main reasons for observing a different efficiency of layouts for E_{DC} and E_{MT} : (1) E_{DC} and E_{MT} reflect different properties of MTs. (2) The decomposition of DC component from the MT is a non-linear procedure, hence the E_{DC} and E_{MT} errors are not related in a simple linear way. Consequently, a lower E_{MT} error does not mean necessarily a lower E_{DC} error. (3) Since the tensile angles of both the strike-slip and dip-slip events are randomly selected between 0° - 90° , this situation is different from the analysis of pure shear events (Ren et al., 2020), which

Table 2

Condition number of the MT inversion for different sensor layouts

Number of sensors	Circular layout	Regular-grid layout	Star-shaped layout	Uniform partial focal-sphere layout	Uniform full focal-sphere layout
25 sensors	3.20	3.52	4.78	6.31	2.86
81 sensors	3.20	3.98	5.98	6.31	2.87

Note that the lowest condition number is achieved for the uniform full focal-sphere layout

means the DC error of the strike-slip events is not always smaller than that of the dip-slip events. The uniform focal-sphere layouts still behave worst.

4. Discussion

The circular layout has the following advantages: (1) The azimuthal coverage is uniform and comprehensive. (2) The condition number, defined as the ratio between the largest and smallest singular values of the matrix \mathbf{G} , is smaller than that for the regular-grid layout and for the star-shaped layout (see Table 2). Dufumier and Rivera (1997) mentioned that the solution may become very unstable for high condition numbers. Interestingly, the condition number is smaller for the uniform full focal-sphere layout than for the circular layout. However, since the hypocentral distances of sensors near the edge of the focal sphere are large in the uniform full focal-sphere layout, the amplitudes are relatively small. Hence, the number of amplitudes with a very low SNR (< 1) is much higher than that in the other layouts (Fig. 10). Consequently, the uniform full focal-sphere layout is handicapped by incorporating too distant sensors. This is the reason why the MT and DC errors of the uniform full focal-sphere layout are always the largest in Table 1 and Fig. 9. At the same time, Fig. 10 shows that the statistics of amplitudes with a low

SNR (< 10) in the circular layout are very similar to the regular-grid layout and the star-shaped layout. Combining the influence of the condition number and the SNR distribution, the circular layout can obtain the highest MT inversion efficiency.

Obviously, the efficiency of the uniform full focal-sphere layout can be improved by removing the distant sensors with a low SNR. For example, we can limit the positions of sensors within Circle 1 as done in the uniform partial focal-sphere layout. As expected, if the distant sensors are removed, the MT and DC errors decrease (Table 1 and Fig. 9). However, this layout is faced with another difficulty: the distribution of sensors is not optimum at angles close to Circle 1, because it is not symmetric. Consequently, the condition number is higher than that for the circular, star-shaped or the regular-grid layouts (Table 2). This leads to a lower accuracy of the results compared to the mentioned more symmetric layouts.

When optimizing circular sensor arrangements, we show that the two-circle layout works better than the one-circle layout. The presence of the central sensor located at the epicentre is quite important in both the layouts. The optimum two-circle layout differs from the one-circle layout by moving some sensors from the circle to the immediate vicinity of the central sensor. This underlines a significant role of observations just at the epicentral area. In the

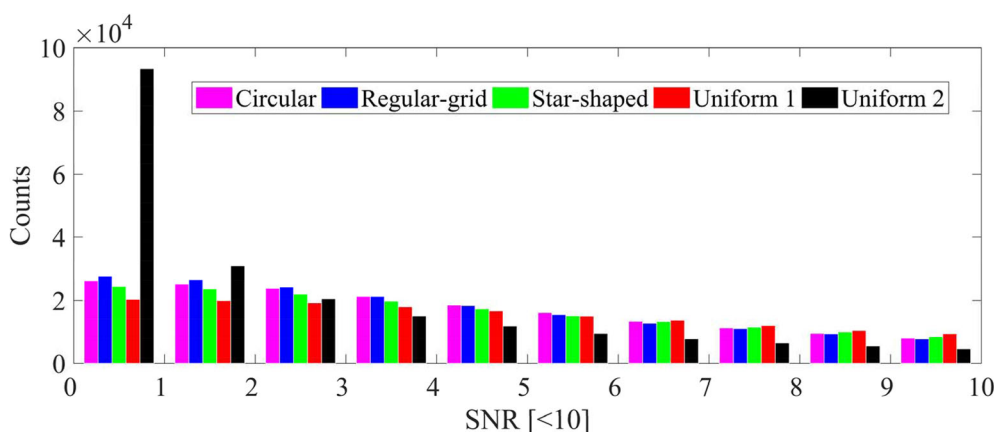


Figure 10

Statistics of the signal-to-noise ratio (SNR) lower than 10 corresponding to the five different layouts with a varying event location. The number of sensors is 25 and no loss of amplitudes is assumed for all 10,000 events. Uniform 1 and Uniform 2 mean the uniform partial and full focal-sphere layouts, respectively

process of optimizing the circular layout, the design strategy for a 9-element array proposed by Schweitzer et al. (2011), which considers the placement of sensors on two circles and at the centre, is also taken into account. However, our circular optimization process takes into account the situations more comprehensively. We also tested the three-circle layouts, but no further improvement has been achieved. The take-off angle to the third circle tends to be identical with that of the second circle nearby the central sensor.

The optimum take-off angle of the outer circle (Circle 1) is always close to 135° . This means that the radius of Circle 1 is the same as depth of the source in homogeneous media. This result is consistent with Ren et al. (2020) who studied optimum regular-grid layouts. In inhomogeneous media with a vertical gradient when rays are concave curved, the radius of Circle 1 should be smaller than depth of the source.

The optimum size of the inner circle (Circle 2) depends on properties of seismic noise. The sensors form a micro-array around the central sensor and the radius of the micro-array should ensure that the observations at individual sensors are affected by seismic noise independently. Since the tests revealed that the position of the central sensor and the radius of the inner circle can slightly vary with no essential effect on the MT errors, the positions of these sensors can be selected based on noise conditions in real experiments.

Among the existing microseismic monitoring systems, the one most similar to our proposed circular layout is the local FORGE seismic network (Pankow et al., 2020; Messimeri et al., 2021). The network consists of five circles with radii of 100 m, 223 m, 500 m, 1180 m, and 2500 m. The injection well is located near the centre of the circle. The system detects events at a depth roughly equal to the radius of the fourth circle (1180 m). The horizontal distance between the event and the injection well is less than 300 m. But in the data processing, the authors do not include the first two circles (radii of 100 m and 223 m) due to their proximity to the injection well and the high level of anthropogenic noise. This emphasizes that effectively reducing the impact of noise on the amplitudes close to the epicentre is very

important when designing the circular layout. Of course, this phenomenon exists also in other layouts.

Compared with other sensor layouts, the circular layout always has the smallest MT error for both random and specified focal mechanisms. However, it does not mean that the circular layout would perform best under all conditions. The analysis performed for random focal mechanisms (Table 1) shows that the inversion errors for the five layouts differ only slightly. Hence, it can happen that the MT errors for the regular-grid layout, star-shaped layout or uniform focal-sphere layouts might be lower than those for the circular layout, if some special focal mechanisms are considered.

5. Conclusions

We have proposed an optimization method for the circular sensor layout for determining the most accurate MTs of microseismic events induced in hydraulic fracturing experiments. The position and size of the sensor network depend on depth of the focal area. An optimum configuration is the two-circle layout characterized by: (1) One central sensor positioned just at the epicentral area, optimally in its centre; (2) a micro-array of sensors distributed around the central sensor. The size of the micro-array should ensure that sensors will be affected independently by seismic noise and the number of sensors should be 1/10 of the total number of sensors; (3) the remaining sensors should evenly be distributed on an outer circle with the take-off angle of about 135° . Optimally, all events should be close to the centre of the circle, but the circular network works efficiently also for other events inside the network. For example, for the radius of the optimum layout of 1000 m, the distance of events from the centre can be up to 500 m. In homogeneous media, the take-off angle of 135° corresponds to a radius of the circle equal to depth of events. In inhomogeneous media with a vertical velocity gradient, the radius of the sensor circle should be smaller than depth of events. The actual value depends on how much the rays are bent by the velocity gradient.

In addition, we tested the efficiency of the two-circle layout for a varying number of sensors ranging

from 10 to 100 and gave the number of sensors on Circle 2 required for the optimal circular layout. As the number of sensors increases, the MT errors are getting smaller. If we enlarge a small number of sensors, the decrease of the errors is significant. If we enlarge a network originally having a high number of sensors, the decrease of the errors is rather small. For a high number of sensors, the errors are also less sensitive to departures of the actual sensor positions from the ideally circular layout.

Taking 25 sensors and 81 sensors as examples, we compared the errors and standard deviations of the MT inversion between the optimum circular layout and the common regular-grid layout, star-shaped layout and uniform focal-sphere layout. The results show that the two-circle layout is always the best irrespective of whether the focal mechanisms are random or of a special type. Hence, the circular layout can achieve more accurate MTs, if the number of sensors in the experiment is fixed. As regards the DC errors E_{DC} , the situation is more complicated, and the circular, regular-grid and star-shaped layouts display a very similar efficiency.

We use the E_{MT} error as the evaluation criterion in the optimization, which can guarantee the accuracy of the MT. However, if some surface monitoring projects pay more attention to other source parameters, such as the accuracy of the focal mechanisms or the percentage of the DC or non-DC components, the evaluation criterion for the layout optimization can easily be modified. Note that we assumed mostly arbitrary focal mechanisms of events. If some area is known for its typical focal mechanisms, then an optimum sensor layout for determining accurate MTs can be found in an analogous way. Also we have to emphasize that we assumed that the focal area is rather small and its position and depth are known. If the area of seismicity is large with a complicated shape as in the multi-well injection experiments, an optimum sensor layout must be found individually and it could be different from that presented in this paper.

Acknowledgements

We thank very much to Editor and two anonymous reviewers for their detailed and constructive comments and suggestions, which helped us to improve the paper considerably.

Funding

The work was supported by the Czech Science Foundation, grants No. 19-06422S and 22-10747S, and by the National Natural Science Foundation of China (51934003).

Declarations

Conflict of interest The authors have no relevant financial or non-financial interests to disclose.

Open Access This article is licensed under a Creative Commons Attribution 4.0 International License, which permits use, sharing, adaptation, distribution and reproduction in any medium or format, as long as you give appropriate credit to the original author(s) and the source, provide a link to the Creative Commons licence, and indicate if changes were made. The images or other third party material in this article are included in the article's Creative Commons licence, unless indicated otherwise in a credit line to the material. If material is not included in the article's Creative Commons licence and your intended use is not permitted by statutory regulation or exceeds the permitted use, you will need to obtain permission directly from the copyright holder. To view a copy of this licence, visit <http://creativecommons.org/licenses/by/4.0/>.

Publisher's Note Springer Nature remains neutral with regard to jurisdictional claims in published maps and institutional affiliations.

REFERENCES

- Anikiev, D., Valenta, J., Staněk, F., & Eisner, L. (2014). Joint location and source mechanism inversion of microseismic events: Benchmarking on seismicity induced by hydraulic fracturing. *Geophysical Journal International*, 198(1), 249–258. <https://doi.org/10.1093/gji/ggu126>
- Baig, A., & Urbancic, T. (2010). Microseismic moment tensors: A path to understanding frac growth. *The Leading Edge*, 29(3), 320–324. <https://doi.org/10.1190/1.3353729>
- Bungum, H., Husebye, E. S., & Ringdal, F. (1971). The NORSAR array and preliminary results of data analysis. *Geophysical Journal International*, 25(1–3), 115–126. <https://doi.org/10.1111/j.1365-246X.1971.tb02334.x>

- Červený, V. (2001). *Seismic ray theory*. Cambridge Univ.
- Chambers, K., Kendall, J. M., Brandsberg-Dahl, S., & Rueda, J. (2010). Testing the ability of surface arrays to monitor microseismic activity. *Geophysical Prospecting*, 58(5), 821–830. <https://doi.org/10.1111/j.1365-2478.2010.00893.x>
- Chen, Y., Huang, L., & EGS Collab Team. (2019). Optimal design of 3D borehole seismic arrays for microearthquakes monitoring in anisotropic media during stimulations in the EGS collab project. *Geothermics*, 79, 61–66. <https://doi.org/10.1016/j.geothermics.2019.01.009>
- Duncan, P. M. (2005). Is there a future for passive seismic? *First Break*, 23, 111–115. <https://doi.org/10.3997/1365-2397.23.6.26577>
- Duncan, P. M., & Eisner, L. (2010). Reservoir characterization using surface microseismic monitoring. *Geophysics*, 75(5), 139–146.
- Dufumier, H., & Rivera, L. (1997). On the resolution of the isotropic component in moment tensor inversion. *Geophysical Journal International*, 131(3), 595–606. <https://doi.org/10.1111/j.1365-246X.1997.tb06601.x>
- Eaton, D. W., & Forouhideh, F. (2011). Solid angles and the impact of receiver-array geometry on microseismic moment-tensor inversion. *Geophysics*, 76(6), WC77–WC85. <https://doi.org/10.1190/geo2011-0077.1>
- Eide, C. H., Schofield, N., Lecomte, I., Buckley, S. J., & Howell, J. A. (2018). Seismic interpretation of sill complexes in sedimentary basins: Implications for the sub-sill imaging problem. *Journal of the Geological Society*, 175(2), 193–209. <https://doi.org/10.1144/jgs2017-096>
- Eisner, L., Duncan, P. M., Heigl, W. M., & Keller, W. R. (2009). Uncertainties in passive seismic monitoring. *The Leading Edge*, 28(6), 648–655. <https://doi.org/10.1190/1.3148403>
- Eisner, L., Hulse, B. J., Duncan, P., Jurick, D., Werner, H., & Keller, W. (2010). Comparison of surface and borehole locations of induced seismicity. *Geophysical Prospecting*, 58(5), 809–820. <https://doi.org/10.1111/j.1365-2478.2010.00867.x>
- Eyre, T. S., & van der Baan, M. (2015). Overview of moment-tensor inversion of microseismic events. *The Leading Edge*, 34(8), 882–888. <https://doi.org/10.1190/tle34080882.1>
- Eyre, T. S., & van der Baan, M. (2017). The reliability of microseismic moment-tensor solutions: Surface versus borehole monitoring. *Geophysics*, 82(6), KS113–KS125. <https://doi.org/10.1190/geo2017-0056.1>
- Kwiatek, G., Martinez-Garzon, P., & Bohnhoff, M. (2016). HybridMT: A MATLAB/shell environment package for seismic moment tensor inversion and refinement. *Seismological Research Letters*, 87(4), 964–976. <https://doi.org/10.1785/0220150251>
- Maxwell, S. C., Rutledge, J., Jones, R., & Fehler, M. (2010). Petroleum reservoir characterization using downhole microseismic monitoring. *Geophysics*, 75(5), 75A129–75A137. <https://doi.org/10.1190/1.3477966>
- Mesimeri, M., Pankow, K. L., & Rutledge, J. (2021). A frequency-domain-based algorithm for detecting microseismicity using dense surface seismic arrays. *Bulletin of the Seismological Society of America*, 111(5), 2814–2824.
- Novitsky, C. G., Holbrook, W. S., Carr, B. J., Pasquet, S., Okaya, D., & Flinchum, B. A. (2018). Mapping inherited fractures in the critical zone using seismic anisotropy from circular surveys. *Geophysical Research Letters*, 45, 3126–3135. <https://doi.org/10.1002/2017GL075976>
- Onnis, L., & Carcione, J. M. (2017). A seismic ray tracing method based on Fibonacci search. *Annals of Geophysics*, 60(2), S0220. <https://doi.org/10.4401/ag-7128>
- Pankow, K., Mesimeri, M., McLennan, J., Wannamaker, P., & Moore, J. (2020). Seismic monitoring at the Utah frontier observatory for research in geothermal energy. Proceedings of the 45th Workshop on Geothermal Reservoir Engineering, Stanford, CA, USA, 10–12.
- Pesicek, J. D., Ciešlik, K., Lambert, M. A., Carrillo, P., & Birkelo, B. (2016). Dense surface seismic data confirm non-double-couple source mechanisms induced by hydraulic fracturing induced non-DC source mechanisms. *Geophysics*, 81(6), KS207–KS217. <https://doi.org/10.1190/geo2016-0192.1>
- Pettitt, W. S. (1998). Acoustic emission source studies of microcracking in rock: University of Keele.
- Pujol, J., & Herrmann, R. B. (1990). A student's guide to point sources in homogeneous media. *Seismological Research Letters*, 61(3–4), 209–224. <https://doi.org/10.1785/gssrl.61.3-4.209>
- Ren, Y., Gao, Y., Wu, S., & Vavryčuk, V. (2020). Optimum size and density of surface grid arrays for retrieving accurate shear-tensile fracturing of microearthquakes. *Geophysical Prospecting*, 68(8), 2347–2360. <https://doi.org/10.1111/1365-2478.12997>
- Schweitzer, J., Fyen, J., Mykkeltveit, S., Gibbons, S. J., Pirl, M., Kühn, D., & Kvaerna, T. (2011). Chapter 9: Seismic arrays, in New IASPEI Manual of Seismological Observatory Practice, P. Bormann (Editor), IASPEI, GFZ German Research Centre for Geosciences, Potsdam, December, 1–80. <https://doi.org/10.2312/GFZ.NMSOP-2>
- Šílený, J., & Vavryčuk, V. (2000). Approximate retrieval of the point source in anisotropic media: Numerical modelling by indirect parametrization of the source. *Geophysical Journal International*, 143, 700–708. <https://doi.org/10.1046/j.1365-246X.2000.00256.x>
- Šílený, J., & Vavryčuk, V. (2002). Can unbiased source be retrieved from anisotropic waveforms by using an isotropic model of the medium? *Tectonophysics*, 356, 125–138. [https://doi.org/10.1016/S0040-1951\(02\)00380-3](https://doi.org/10.1016/S0040-1951(02)00380-3)
- Šílený, J. (2009). Resolution of non-double-couple mechanisms: Simulation of hypocenter mislocation and velocity structure mismodeling. *Bulletin of the Seismological Society of America*, 99(4), 2265–2272. <https://doi.org/10.1785/0120080335>
- Staněk, F., Eisner, L., & Moser, T. J. (2014). Stability of source mechanisms inverted from P-wave amplitude microseismic monitoring data acquired at the surface. *Geophysical Prospecting*, 62(3), 475–490. <https://doi.org/10.1111/1365-2478.12107>
- Staněk, F., Eisner, L., & Vesnaver, A. (2017). Theoretical assessment of the full-moment-tensor resolvability for receiver arrays used in microseismic monitoring. *Acta Geodynamica et Geomaterialia*, 2, 235–240. <http://dx.doi.org/https://doi.org/10.13168/AGG.2016.0006>
- Stierle, E., Vavryčuk, V., Šílený, J., & Bohnhoff, M. (2014a). Resolution of non-double-couple components in the seismic moment tensor using regional networks: 1. A synthetic case study. *Geophysical Journal International*, 196(3), 1869–1877. <https://doi.org/10.1093/gji/ggt502>
- Stierle, E., Bohnhoff, M., & Vavryčuk, V. (2014b). Resolution of non-double-couple components in the seismic moment tensor using regional networks: 2. Application to aftershocks of the 1999 Mw 7.4 Izmit earthquake. *Geophysical Journal International*, 196(3), 1878–1888. <https://doi.org/10.1093/gji/ggt503>

- Tsuji, T., Hino, R., Sanada, Y., Yamamoto, K., Park, J.-O., No, T., Araki, E., Bangs, N., von Huene, R., Moore, G., & Kinoshita, M. (2011). In situ stress state from walkaround VSP anisotropy in the Kumano basin southeast of the Kii Peninsula, Japan. *Geochemistry, Geophysics, Geosystems*, 12(9), Q0AD19. <https://doi.org/10.1029/2011GC003583>
- Vavryčuk, V. (1997). Elastodynamic and elastostatic Green tensors for homogeneous weak transversely isotropic media. *Geophysical Journal International*, 130(3), 786–800. <https://doi.org/10.1111/j.1365-246X.1997.tb01873.x>
- Vavryčuk, V. (2001). Inversion for parameters of tensile earthquakes. *Journal of Geophysical Research: Solid Earth*, 106, 16339–16355. <https://doi.org/10.1029/2001JB000372>
- Vavryčuk, V. (2003a). Parabolic lines and caustics in homogeneous weakly anisotropic solids. *Geophysical Journal International*, 152, 318–334. <https://doi.org/10.1046/j.1365-246X.2003.01845.x>
- Vavryčuk, V. (2003b). Behavior of rays near singularities in anisotropic media. *Physical Review B*, 67(5), 054105. <https://doi.org/10.1103/PhysRevB.67.054105>
- Vavryčuk, V. (2007). Ray velocity and ray attenuation in homogeneous anisotropic viscoelastic media. *Geophysics*, 72(6), D119–D127. <https://doi.org/10.1190/1.2768402>
- Vavryčuk, V. (2008). Real ray tracing in anisotropic viscoelastic media. *Geophysical Journal International*, 175, 617–626. <https://doi.org/10.1111/j.1365-246X.2008.03898.x>
- Vavryčuk, V. (2011). Tensile earthquakes: Theory, modeling, and inversion. *Journal of Geophysical Research*, 116, B12320. <https://doi.org/10.1029/2011JB008770>
- Vavryčuk, V., Adamová, P., Doubravová, J., & Jakoubková, H. (2017). Moment tensor inversion based on the principal component analysis of waveforms: Method and application to microearthquakes in West Bohemia, Czech Republic. *Seismological Research Letters*, 88(5), 1303–1315. <https://doi.org/10.1785/0220170027>
- Vavryčuk, V., Hrubcová, A., Brož, M., Málek, J., & ALP 2002 Working Group. (2004). Azimuthal variation of Pg velocity in the Moldanubian, Czech Republic: Observations based on a multi-azimuthal common-shot experiment. *Tectonophysics*, 387(1–4), 189–203. <https://doi.org/10.1016/j.tecto.2004.06.015>
- Viegas, G., & Baig., A., Coulter, W., & Urbancic, T. (2012). Effective monitoring of reservoir-induced seismicity utilizing integrated surface and downhole seismic networks. *First Break*, 30, 77–81. <https://doi.org/10.3997/1365-2397.30.7.60347>
- Wessels, S. A., De La Pena, A., Kratz, M., Williams-Stroud, S., & Jbeili, T. (2011). Identifying faults and fractures in unconventional reservoirs through microseismic monitoring. *First Break*, 29(7), 99–104. <https://doi.org/10.3997/1365-2397.29.7.51919>
- Willemann, R. J. (1993). Cluster analysis of seismic moment tensor orientations. *Geophysical Journal International*, 115(3), 617–634. <https://doi.org/10.1111/j.1365-246X.1993.tb01484.x>
- Wust-Bloch, G. H., & Joswig, M. (2006). Pre-collapse identification of sinkholes in unconsolidated media at Dead Sea area by ‘nanoseismic monitoring’ (graphical jackknife location of weak sources by few, low-SNR records). *Geophysical Journal International*, 167, 1220–1232. <https://doi.org/10.1111/j.1365-246X.2006.03083.x>
- Zhang, Y., Eisner, L., Barker, W., Mueller, M. C., & Smith, K. (2011). Consistent imaging of hydraulic fracture treatments from permanent arrays using a calibrated velocity model. In *Third EAGE Passive Seismic Workshop-Actively Passive, Athens, Greece*. <https://doi.org/10.3997/2214-4609.20145327>

(Received August 13, 2021, revised June 21, 2022, accepted July 27, 2022, Published online August 22, 2022)